Degenerate four-wave mixing in silicon hybrid plasmonic waveguides

THORIN J. DUFFIN[1,2,†], MICHAEL P. NIELSEN[1,†], FERNANDO DIAZ[3], STEFANO PALOMBA[3,*], STEFAN A. MAIER[1], AND RUPERT F. OULTON[1,*]

[1] The Blackett Laboratory, Department of Physics, Imperial College London, London SW7 2AZ, United Kingdom
[2] National University of Singapore Graduate School of Integrative Sciences and Engineering, National University of Singapore, Singapore 119077, Singapore
[3] Institute of Photonics and Optical Science (IPOS), School of Physics, University of Sydney, Sydney, NSW 2006, Australia
[†] Authors with equal contribution
[*] Corresponding authors: stefano.palomba@sydney.edu.au, r.oulton@imperial.ac.uk

Compiled November 3, 2015

Silicon-based plasmonic waveguides show high confinement well beyond the diffraction limit. Various devices have been demonstrated to outperform their dielectric counterparts at micrometre scales, such as linear modulators, capable of generating high field confinement and improving device efficiency by increasing access to nonlinear processes, limited by ohmic losses. By using hybridised plasmonic waveguide architectures and nonlinear materials, silicon-based plasmonic waveguides can generate strong nonlinear effects over just a few wavelengths. We have theoretically investigated the nonlinear optical performance of two hybrid plasmonic waveguides (HPWG) with three different nonlinear materials. Based on this analysis, the hybrid gap plasmon waveguide (HGPW), combined with the DDMEBT nonlinear polymer, shows a four-wave mixing (FWM) conversion efficiency of $-16.4dB$ over a $1\mu m$ propagation length, demonstrating that plasmonic waveguides can be competitive with standard silicon photonics structures over distances three orders of magnitude shorter.

OCIS codes: *(130.7405) Wavelength conversion devices, (190.4380) Nonlinear optics, four-wave mixing, (240.6680) Surface plasmons*

http://dx.doi.org/10.1364/ao.XX.XXXXXX

Silicon-based plasmonic waveguides provide high field confinement, making them good candidates to integrate sub-diffraction limit propagation into contemporary silicon photonics and nano-electronics[1–5]. Plasmonic waveguides enable sub-diffraction propagation[6, 7] and nano-focussing[8–11], which allows efficient nonlinear optical generation for ultrafast optical signal processing and data transfer[1]. This enhanced efficiency can be utilised to reduce the device size of linear modulators from centimetre scales in silicon photonic modulators[12] down to the order of micrometres[13]. Nevertheless, semiconductor plasmonic waveguides are still affected by prohibitive ohmic losses, which limit the propagation length to tens of wavelengths or less. However, it has been shown that these losses can be partially reduced by incorporating a low refractive index material between the metal and high refractive index semiconductor, forming a hybrid plasmonic waveguide (HPWG)[6]. HPWGs exploit the high modal confinement of plasmonic waveguides with reduced but omnipresent losses.

Although both electro-optical[13] and all-optical[14] modulation have been examined in silicon plasmonic waveguides, an important wavelength conversion phenomenon for signal processing – four-wave mixing (FWM) – remains unexplored. A consequence of the Kerr effect-induced intensity-dependent refractive index change, FWM involves the interaction of two pump photons that generates two new photons at different frequencies[15]. Degenerate FWM, where both input pump photons have the same frequency, has been shown to be an efficient method to transfer information from the input pump beam to the output idler beam with almost perfect fidelity[19, 20].

An active plasmonic material with very low refractive index but very high Kerr index is desirable to enhance nonlinearities. A low refractive index reduces propagation losses[21], and a high Kerr index amplifies a material's nonlinear optical response[15]. Some organic materials have been shown to be capable of high optical nonlinearities, due to delocalised π-bonds which produce Kerr indices independent of linear refractive index[15], in contrast to inorganic materials that have a close relationship between their linear index and their Kerr index. These nonlinear organic materials have already been effectively utilised for nonlinear wavelength conversion and modulation in photonics through the silicon-organic hybrid slot waveguides[16–18]. Such materials can offer the high nonlinear effects and low refractive indices that are advantageous for HPWGs. In this letter, we examine two different HPWGs: the metal-insulator-semiconductor plasmonic waveguide (MIS)[5] (Fig. 1a) and the hybrid gap plasmon waveguide (HGPW)[11] (Fig. 1b). These platforms offer the potential of generating higher field confinement and lower propagation loss than other silicon plasmonic waveguides, making them suitable for nonlinear optical signal generation.

In order to understand the relationship between high confine-

ment and high losses for different active materials, we need to examine how each influences FWM as the pulses traverse the waveguide. In degenerate FWM, a strong initial pump pulse with frequency ω_1 interacts with a signal probe pulse at a frequency ω_2. This results in both the potential amplification of the signal pulse, as well as the generation of a new idler conjugate pulse at ω_3 that can be related back to the pump pulse by $2\omega_1 = \omega_2 + \omega_3$[19]. For degenerate FWM, a set of three coupled equations derived from the non-linear Schrödinger equation (NLSE) gives the complete description of the pulse propagation down the waveguide. The three coupled equations describe how the pump pulse A_1 interacts with a seeded signal pulse A_2 and the two generate a third idler pulse A_3. These three equations differ only by their phase matching term (PM) and can be given by Eq. 1 (with $j = 1, 2, 3$):

$$\frac{dA_j}{dz} + \sum_{n=2}^{\infty} \frac{i^n \beta_{n,j}}{n!} \left(\frac{\partial A_j}{\partial T}\right)^n = \left[-\frac{1}{2}(\alpha_j + \alpha_{fc,j}) + i\frac{2\pi}{\lambda_j}\delta_{nfc,j}\right] A_j + i\widetilde{\gamma}_j \left(1 + \frac{i}{\omega_j}\frac{\partial}{\partial T}\right) \left|A_j\right|^2 A_j + 2iA_j \sum_{k\neq j} \widetilde{\gamma}_{j,k} |A_k|^2 + PM_j, \tag{1}$$

where T denotes the retarded time $T = t - z\beta_1$ and $PM_1 = 2i\gamma_1 A_1^* A_2 A_3 exp(i\Delta kz)$, $PM_2 = i\gamma_2 A_3^* A_1^2 exp(-i\Delta kz)$ and $PM_3 = i\gamma_3 A_2^* A_1^2 exp(-i\Delta kz)$. $\beta_{n,j}$ on the left of Eq. 1 denotes the nth order dispersion for the pulse A_j. Dispersion up to the third order ($n = 3$) is considered, and all dispersion values were calculated at each wavelength using ComSol. On the right, linear absorption loss is given by α_j and the free carrier absorption $\alpha_{fc,j}$ where $\alpha_{fc,j} = \sigma_j N_{fc}$, with σ_j as the free carrier absorption coefficient given by $\sigma_j = 1.45 \times 10^{-21}(\lambda_j/\lambda_0)^2[\mathrm{m}^2]$ and N_{fc} is the free carrier density. The free carrier-induced refractive index change is given by $\delta_{nfc,j}$ and can be related to the free carrier density by $\delta_{nfc,j} = \zeta_j N_{fc}$ where $\zeta_j = -1.35 \times 10^{-27}(\lambda_j/\lambda_0)^3[\mathrm{m}^2]$, with λ_0 as the initial pump wavelength. The free carrier density $N^{n+1/2}$ can be calculated approximately at each temporal step using[22]

$$N_{fc}^{n+\frac{1}{2}}(z,t) \approx \frac{2\tau_c - \Delta t}{2\tau_c + \Delta t} N_{fc}^{n-\frac{1}{2}} + \frac{\tau_c \Delta t}{2\tau_c + \Delta t} \frac{\beta_{TPA}}{hc} \sum_j \lambda_j \left|A_j^n(z,t)\right|^4, \tag{2}$$

where the free carrier lifetime $\tau_c \approx 1ns$[23]. The second term on the right of the equality in Eq. 1 describes the self-phase modulation (SPM) of each pulse. The nonlinear coefficient $\widetilde{\gamma}_j$ is computed for each material and scaled by the respective fractional energy $E_{f,j}$ with an effective nonlinear coefficient $\widetilde{\gamma}_{eff} = \sum \widetilde{\gamma}_j E_{f,j}$, with each constituent $\widetilde{\gamma}_j$ given by[19, 24]

$$\widetilde{\gamma}_j = \frac{\omega_j n_2}{c A_m} + i\frac{\beta_{TPA}}{2A_m}, \tag{3}$$

where n_2 is the Kerr index of the material, A_m is the effective mode area, β_{TPA} is the two-photon absorption (TPA) coefficient, and c is the speed of light. The final two terms in Eq. 1 describe the cross-phase modulation (XPM) and PM of each pulse, where the PM of the pulse contains the propagation distance z and phase-mismatch term Δk which relates to the propagation constants for each pulse according to $\Delta k = k_2 + k_3 - 2k_1$ where $k_j = \widetilde{n}_j \omega_j / c$ and the effective refractive index $\widetilde{n}_j = n_j + \Delta n_j$ with Δn_j as the change in refractive index due to waveguiding[19]. However, this is of little impact as a propagation distance of only a few wavelengths is examined. SRS terms are absent from Eq. 1 as Raman effects were found to be negligible, as was an XPM term in Eq. 2. A term for third harmonic generation is also neglected[25] as there is little overlap between the fundamental and third harmonic field profiles in the proposed structures.

Fig. 1 depicts the two silicon hybrid plasmonic waveguide architectures studied in this letter: a) MIS and b) HGPW and their respective electromagnetic modal distributions c) and d). The MIS waveguide is made of a silicon-on-insulator (SOI) standard strip waveguide with a spacer layer of thickness S, topped with a metal strip of thickness M all with a width $W1$. With the given dimensions, the waveguide supports predominantly transverse-magnetic (TM) modes. The HGPW architecture discussed in [11] differs from the MIS waveguide by patterning a metal gap of width $W2$ atop the spacer layer and not etching the sides. The HGPW waveguide supports predominantly transverse-electric (TE) modes. Both geometries allow high confinement due to the metal regions loading the underlying slab, raising the local effective index contrast and generating strong lateral confinement[11].

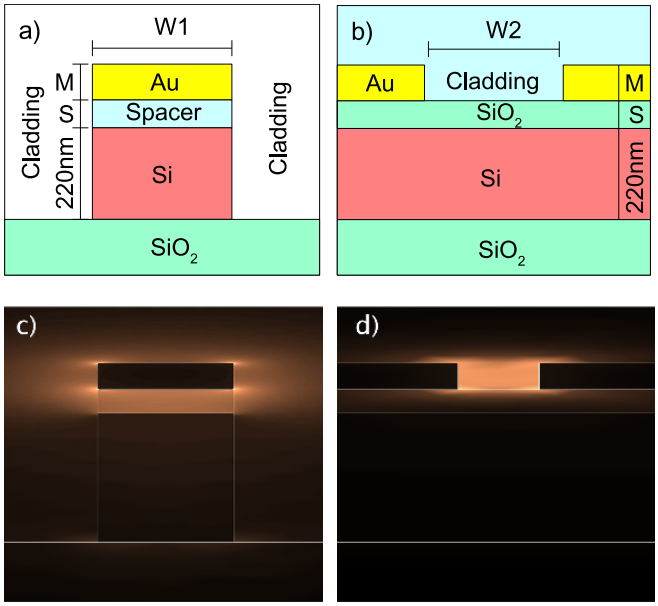

Fig. 1. a) The MIS geometry where the active material fills the spacer layer. b) The HGPW waveguide where the active material fills the gap and cladding. c) Mode diagram of the MIS geometry - W1=50nm, S=20nm, M=40nm. d) Mode diagram of HGPW geometry, W2=20nm, S=20nm, M=40nm.

Holding all other parameters constant and varying the width in each waveguide, the highest nonlinear response was at a width of $W1 = 50nm$ for the MIS waveguide and $W2 = 10nm$ for the HGPW gap. In each geometry, metal film thickness $M = 50nm$, spacer layer thickness $S = 20nm$, and the silicon layer thickness of $220nm$, corresponding to a standard SOI substrate with a $3\mu m$ buried oxide layer. The width $W1 = 50nm$ is the smallest width that still supports a bound mode in the MIS waveguide. On the other hand, the HGPW waveguide can support a mode with an infinitesimally small gap, but widths smaller than $W2 = 10nm$ are extremely difficult to fabricate, even with template stripping processes. Three nonlinear materials were examined as potential active plasmonic materials,

placed in the spacer for the MIS geometry and in the cladding for the HGPW: DDMEBT[18], DAN2[26] and silicon nitride. Each material was chosen either for its potentially high nonlinear response (DDMEBT, DAN2) or for its CMOS compatibility (Si_3N_4). Table 1 gives each material's refractive index n, Kerr index n_2, TPA coefficient β_{TPA} and the corresponding wavelengths.

Table 1. Optical constants used

Material	$\lambda(nm)$	n	$n_2(m^2/W)$	$\beta_{TPA}(cm/GW)$
DDMEBT [18]	1550	1.8	1.7e-17	0
DAN2 [26]	1579	1.645	1.1e-17	1
Si_3N_4	1600	2.05	2.4e-19	0
Silicon	1550	3.458	2.6e-18	0.74
SiO_2	1550	1.524	2.36e-20	0
Au	1550	0.56 -11.12i	7.8e-17	0

The effective mode area for each geometry is calculated using the definition of mode area A_2 from [7] as it takes into account the total energy density of the mode, allowing characterisation of the complete electromagnetic size of the mode. Fig. 2 shows the vacuum diffraction limit-normalised mode area A_m/A_0 . The three nonlinear materials in the HPGW are compared with DDMEBT as the spacer layer in the MIS waveguide, and both architectures are compared with a typical SOI strip waveguide ($450nm \times 220nm$). Fig. 2 highlights the low mode area of DDMEBT in the HGPW and shows that both HGPW and MIS waveguides are capable of higher sub-diffraction confinement than the SOI strip waveguide. Modal characteristics of each waveguide were calculated using mode-solving algorithms in ComSol. Calculating propagation length L_m, for DDMEBT in the MIS waveguide $L_m = 3.5\mu m$. In the HGPW geometry, the propagation length is $L_m = 1.7\mu m$ for DDMEBT, $L_m = 1.2\mu m$ for DAN2 and $L_m = 2.6\mu m$ for Si_3N_4. The strip SOI waveguide has a propagation length $L_m = 2cm$[27].

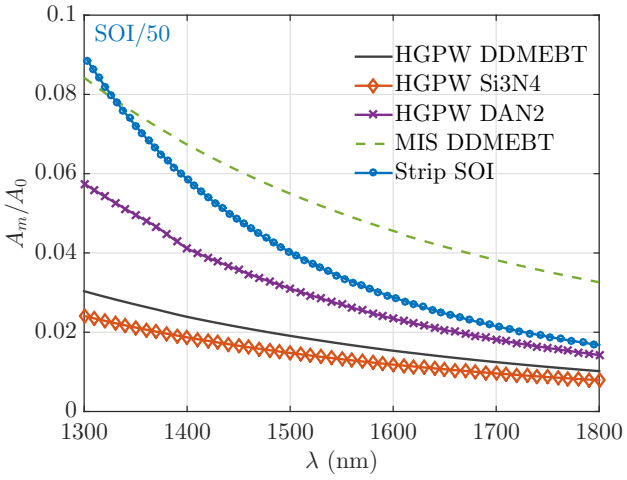

Fig. 2. Diffraction-limit normalised mode area for different waveguide architectures and materials.

FWM is simulated in each geometry using hyperbolic-secant input pulses with varying peak input power P_1. Fig. 3a shows the spectra for the HGPW geometry clad with DDMEBT, propagating down a waveguide of length $z = 10\mu m$, with a pump pulse A_1 at a central frequency of $\lambda_1 = 1550nm$ with a peak power $P_1 = 5W$, an initial signal pulse A_2 at a central frequency of $\lambda_2 = 1363nm$ with a peak power $P_2 = 0.1W$, with an idler pulse at a central frequency $\lambda_3 = 1796nm$. Each pulse has a pulse width $\tau = 0.3ps$. The entire power spectrum is normalised to the input peak pump power P_1. The highest power in the idler pulse can be seen at $z = 1\mu m$. Fig. 3b gives the conversion efficiency (CE) for the same waveguide, emphasising the losses seen in Fig. 3a as each pulse reaches $z = 50\mu m$. It also shows the improved efficiency for an SOI strip waveguide as the propagation length increases, where the SOI strip waveguide surpasses the CE of the HGPW with DDMEBT at $z = 14\mu m$.

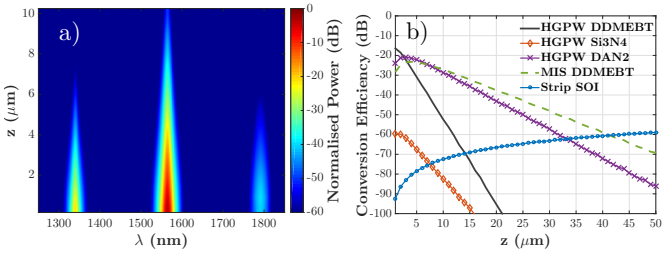

Fig. 3. a) Complete spectra for FWM in an HGPW waveguide over $10\mu m$, normalised to the input peak pump power P_1. Signal on the left, pump in the centre and idler on the right. b) CE as a function of propagation distance.

The logarithmic ratio of the output idler pulse A_{3f} to the initial signal input energy A_{2i} gives the CE η[dB] $= 10\ \log_{10}(A_{3f}/A_{2i})$[19]. The CE gives an indication of the strength of FWM through the waveguide. Fig. 4 plots the CE for each geometry and active material. The initial signal peak power is kept at $P_2 = 0.1W$ and the input peak pump power is varied from $P_1 = 0.1W$ to $P_1 = 6W$. Each CE is calculated over a distance of $z = 1\mu m$. DDMEBT in the HGPW geometry gives highest CE, followed by the same material in the MIS. The second highest material CE is given by DAN2, slightly below DDMEBT in the MIS. Silicon nitride follows with significantly worse efficiency, but still better than the SOI strip waveguide.

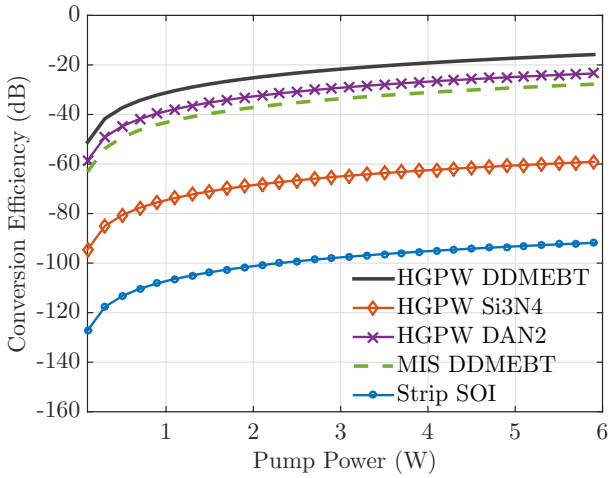

Fig. 4. CE as a function of pump power in watts, calculated over $1\mu m$.

The HGPW geometry with DDMEBT cladding gives the high-

est CE when $z = 1\mu m$. The HGPW offers a smaller mode area (Fig. 2) than the MIS geometry and higher field confinement due to its ability to maintain a mode at widths that MIS cannot access. DDMEBT has the highest Kerr index of the three nonlinear materials as well as a negligible TPA coefficient, and when coupled with the HGPW, offers the highest mode confinement and strongest nonlinear response. For a peak input pulse into the HGPW waveguide with DDMEBT cladding at $\lambda_1 = 1550nm$, $\lambda_2 = 1363nm$, $P_1 = 5.5W$, $P_2 = 0.1W$, the maximum CE $\eta_{max} = -16.4dB$.

DAN2 and Si_3N_4 return lower CEs. At length scales of only a few micrometres, material nonlinear properties have a stronger influence than linear properties on FWM. Although DAN2 has lower absorption losses than DDMEBT, the reduced Kerr index, larger mode area and larger TPA coefficient return a lower CE. Similarly, Si_3N_4 has a lower Kerr index by two orders of magnitude which leads to lower CE. However, Fig. 3b shows that over longer propagation lengths, DDMEBT in the HGPW becomes less efficient than the other materials or DDMEBT in the MIS, emphasising that the nonlinear strength of the HGPW geometry with DDMEBT cladding is not sustainable for longer lengths.

Fig. 4 further shows the comparatively low efficiency of an SOI strip waveguide over $z = 1\mu m$. Typical SOI FWM takes place over length scales of three orders of magnitude longer, and at such short lengths, SOI strip waveguides are not effective. For typical SOI FWM lengths, phase-matching is an important condition that would cause high walk-off in the other materials used here, but plasmonic FWM distances are insufficient for significant walk-off to occur, allowing access to a wider range of materials and wavelengths not suited for phase-matching.

Our results are competitive with other ultrafast silicon photonic FWM experiments, as Table 2 shows. At the same peak powers and pulse widths, we can only recover CEs 2-3 times lower than the other experiments due to lower propagation lengths. However, raising the peak power sees the CE increase to a competitive level. Typical silicon waveguide experiments avoid peak powers of more than a few watts due to high TPA, but DDMEBT's negligible TPA coefficient allows access to higher input powers without losses due to TPA or significant free carrier effects. The pump pulse energy E_1 is closer to other experiments as the high powers are pumped for a fraction of a picosecond. This demonstrates that micrometre scale FWM in silicon hybrid plasmonic waveguides can offer competitive efficiencies to contemporary silicon photonic waveguides over similar distances.

Table 2. CEs of ultrafast silicon FWM

Paper	$P_1(mW)$	$P_2(mW)$	$L(mm)$	$\tau(ps)$	$E_1(pJ)$	$CE(dB)$
Lavdas et al. [28]	200	20	60	0.5	0.1	−25
Salem et al. [29]	200	25	18	33	6.6	−20
Pu et al. [30]	200	0.3	3	1	0.2	−16.5
This work	5500	100	0.001	0.3	1.7	−16.4

This letter has shown that wavelength conversion via FWM can be achieved over distances of less than a wavelength – distance scales that render phase-matching unnecessary – with comparable CEs to contemporary ultrafast pulsed silicon photonics experiments three orders of magnitude longer, and with a maximum CE $\eta_{max} = -16.4dB$. The HGPW geometry with DDMEBT cladding offers the highest CE due to large Kerr index and high mode confinement combined with the reduced-ohmic loss ability of a hybridised waveguide. Furthermore, we demonstrate that nonlinear effects have a stronger influence on FWM than linear loss over the scale of a few micrometres. These results suggest that nonlinear effects could be utilised over wavelength-scale distances in silicon hybrid plasmonic waveguides, which could contribute to sub-diffraction optical propagation technologies, broadening the range of contemporary silicon photonics.

FUNDING INFORMATION

EPSRC Fellowship (EP/I004343/1); EPSRC Reactive Plasmonics Programme (EP/M013812/1); Leverhulme Trust; Marie Curie IRG (PIRG08-GA-2010-277080); Australian Research Council (ARC) Discovery Project (DP150100779).

REFERENCES

1. I. D. Rukhlenko, M. Premaratne, and G. P. Agrawal, Opt. Express **19**, 206 (2011).
2. I. Goykhman, B. Desiatov, and U. Levy, Appl. Phys Lett. **97**, 141106 (2010).
3. M. Nielsen, A. Ashfar, K. Cadien, and A. Elezzabi, Opt. Mat. **36**, 294 (2013).
4. L. Y. M. Tobing, L. Tjahjana, and D. Hua Zhang, Appl. Phys. Lett **101**, 041117 (2012).
5. M. P. Nielsen and A. Y. Elezzabi, Appl. Phys. Lett. **103**, 051107 (2013).
6. R. F. Oulton, V. J. Sorger, D. A. Genov, D. F. P. Pile, and X. Zhang, Nature Phot. **2**, 496 (2008).
7. R. F. Oulton, G. Bartal, D. F. P. Pile, and X. Zhang, New J. of Phys. **10**, 105018 (2008).
8. H. Choo, M. K. Kim, M. Staffaroni, T. J. Seok, J. Bokor, S. Cabrini, P. J. Schuck, M. C. Wu, and E. Yablonovitch, Nature Phot. **6**, 838 (2012).
9. D. K. Gramotnev and S. I. Bozhevolnyi, Nature Phot. **8**, 13 (2013).
10. M. Stockman, Phys. Rev. Lett. **93**, 137404 (2004).
11. L. Lafone, T. P. H. Sidiropoulos, and R. F. Oulton, Opt. Lett. **39**, 4356 (2014).
12. G. T. Reed, G. Mashanovich, F. Y. Gardes, and D. J. Thomson, Nature Phot. **4**, 518 (2010).
13. V. J. Sorger, R. F. Oulton, R. M. Ma, and X. Zhang, MRS Bull. **37**, 728 (2012).
14. M. P. Nielsen and A. Y. Elezzabi, Opt. Express **21**, 20274 (2013).
15. R. W. Boyd, (Elsevier, 2008).
16. A. Trita, C. Lacava, P. Minzioni, J. Colonna, P. Gautier, J. Fedeli, and I. Cristiani, Appl. Phys. Lett. **99**, 191105 (2011).
17. L. An, H. Liu, Q. Sun, N. Huang, and Z. Wang, Appl. Opt. **53**, 4886 (2014)
18. C. Koos, P. Vorreau, T. Vallaitis, P. Dumon, W. Bogaerts, R. Baets, B. Esembeson, I. Biaggio, T. Michinobu, F. Diederich, W. Freude, and J. Leuthold, Nature Phot. **3**, 216 (2009).
19. G. P. Agrawal, (Academic Press, New York, 2001), 3rd ed.
20. H. Fukuda, K. Yamada, T. Shoji, M. Takahashi, T. Tsuchizawa, T. Watanabe, J. Takahashi, and S. Itabashi, Opt. Express **13**, 4629 (2005).
21. S. Maier, (Springer, Bath, 2007), 1st ed.
22. N. Suzuki, J. of Light. Tech. **25**, 2495–2501 (2007).
23. Q. Lin, O. J. Painter, and G. P. Agrawal, Opt. Express **15**, 16604 (2007).
24. S. Afshar, V. T. M. Monro, and C. Martin de Sterke, Opt. Ex. **21**, 18558 (2013).
25. T. Wu, P. Shum, X. Shao, T. Huang, and Y. Sun, Opt. Ex. **22**, 24367 (2014).
26. M. B. Marques, G. Assanto, G. I. Stegeman, G. R. Möhlmann, E. W. P. Erdhuisen, and W. H. G. Horsthuis, Appl. Phys. Lett. **58**, 2613 (1991).
27. L. Yin and G. P. Agrawal, Opt. Lett. **32**, 2031 (2007).
28. S. Lavdas, S. Zhao, J. B. Driscoll, R. R. Grote, R. M. Osgood, and N. C. Panoiu, Opt. Lett. **39**, 4017–20 (2014).
29. R. Salem, M. A. Foster, A. C. Turner, D. F. Geraghty, M. Lipson, and A. L. Gaeta, Nature Phot. **2**, 35–38 (2007).
30. M. Pu, H. Hu, M. Galili, H. Ji, C. Peucheret, L. K. Oxenløwe, K. Yvind, P. Jeppesen, and JM. Hvam, IEEE Phot. Tech. Lett. **23**, 1409–1411 (2011).